frontiers | Frontiers in Energy Research

TYPE Original Research
PUBLISHED 28 October 2022
DOI 10.3389/fenrg.2022.995034

OPEN ACCESS

EDITED BY
Salah Kamel,
Aswan University, Egypt

REVIEWED BY
Sahaj Saxena,
Thapar Institute of Engineering and Technology, India
Ravita Lamba,
Malaviya National Institute of Technology, India

*CORRESPONDENCE
K. Palanisamy,
kpalanisamy@vit.ac.in

SPECIALTY SECTION
This article was submitted to Solar Energy, a section of the journal Frontiers in Energy Research

RECEIVED 15 July 2022
ACCEPTED 21 September 2022
PUBLISHED 28 October 2022

CITATION
Kumar GVB and Palanisamy K (2022), Energy management of renewable energy-based microgrid system with HESS for various operation modes. *Front. Energy Res.* 10:995034. doi: 10.3389/fenrg.2022.995034

Energy management of renewable energy-based microgrid system with HESS for various operation modes

G. V. Brahmendra Kumar and K. Palanisamy*

School of Electrical Engineering, Vellore Institute of Technology, Vellore, India

This paper proposes a ramp-rate control approach for a grid-connected MG with a hybrid energy storage system. Distributed energy sources (DERs), such as solar photovoltaic (PV) and wind, combined with energy storage (ES) and controllable loads, are critical to a power grid that can handle the intermittent nature of renewable energy sources. Therefore, the complexity of the system is increasing as researchers move towards a more renewable based power grid. An energy management system (EMS) for microgrids must consider the power available in RESs as well as the storage capacity of energy storage devices (ESSs). Modern MGs include a wide range of converters for a variety of applications, including distributed generation interconnection, grid integration, energy storage management systems, and demand management, among others. So, the ramp-rate control smooths fluctuations in photovoltaic power, which increases system reliability. In the proposed system, 80 V DC is used to supply high and low power DC loads. The suggested system can extract the maximum amount of energy from RESs, maintain efficient ESS management, and achieves quick DC-link voltage regulation with settling time of 230 ms throughout all operating modes. These conditions are met by the energy management system, which gives the MG with operational capability and ensures its reliability. The MG with proposed features and EMS was validated using the MATLAB/Simulink environment, and results were obtained using the Hardware-in-the-Loop (HIL) experimental test bench. The proposed small-scale RES-based MG can be used to develop and test algorithms for a wide range of MG applications.

KEYWORDS

renewable energy resources, solar PV, ramp-rate control, microgrid, energy management, hybrid energy storage system

Abbreviations: BW, bandwidth; BS, battery storage; CCL, current control loop; CLTF, closed loop transfer function; DG, distributed generation; DER, distributed energy sources; DPM, deficit power mode; EPM, excess power mode; ESS, energy storage system; EMS, energy management system; MG, microgrid; OLTF, open loop transfer function; PV, photovoltaic; RR, ramp-rate control; SC, super-capacitor; SISO, single-input single-output; SoC, state of charge; UPF, unity power factor; VSC, voltage source converter; VCL, voltage control loop.

1 Introduction

Current power grids are struggling to cope with the increasing electricity demand. A MG interconnected RESs and loads have emerged as an attractive alternative to traditional fossil fuel-based power generation to reduce operational and environmental costs (Brahmendra Kumar and Palanisamy, 2019). On the other hand, renewable energy is sporadic in nature. Therefore, MGs cannot be relied upon to function continuously (Zia et al., 2018).

As a result of this problem, several solutions have been proposed. MGs, for example, may be permanently linked to the main grid to compensate for any energy shortfalls. This initiative is not environmentally friendly and may lead to higher energy costs for MGs, as any energy deficit should be mitigated by obtaining conventional power from the main grid despite high electricity prices of the main grid. Moreover, storage systems can be used in combination with RES to store excess energy, which can be released when demand is low or when the price of electricity from the main grid is high (Yi et al., 2017). However, it is not a good practice to rely solely on ESSs due to their limited capacity, high maintenance costs, and losses during the charging and discharging processes.

There have been many changes in smart grid technology over the past few years, and one of them is energy cooperation between MGs, which has been suggested as a new way to implement MGs more reliably and at a lower cost (Gundumalla and Eswararao, 2018). Energy cooperation allows MGs to share power with those with surplus power. Then, it is important to ensure that the amount of energy each MG draws from the main grid, the amount each MG charges and the amount it discharges from the ESS, all work together (Sahoo et al., 2018). This means that MGs must work together to improve their energy management.

The most common hybrid RES are solar and wind power. A variety of control techniques are used to ensure efficient transfer of power in hybrid RESs. Energy conversion systems and converters used at different locations in the entire energy system affect the system design, which requires a lot of interest and research in this area (Kumar and Palanisamy, 2020). A PV-battery based hybrid MG system is proposed in (Yi et al., 2017). In this, the BS balances the power between the DC link and the AC link under all conditions, which places additional strain on the BS. Hence, the system cost increases to handle peak demand and battery life is shortened. In (Anilkumar et al., 2020), various load demand profiles and weather data were analyzed to evaluate the performance of a hybrid energy system. It discussed irradiation changes based on atmospheric conditions and effects on PV power profile. Improve DC grid voltage regulation for standalone DC MGs with battery and SC as discussed in (Sathishkumar et al., 2012; Kumar et al., 2020). But more settling time is required to restore a constant DC link voltage when the load changes.

In (Ouammi et al., 2015; Wang et al., 2015; Mahmood and Jiang, 2019; Fu et al., 2022), a single MG or a group of MGs operating independently of each other were studied. These studies focus on the off-line EMS problem by assuming that RES generation and load demand are deterministic or known in advance. Stochastic RES generation and load models were used to solve the online EMS problem. But these do not take into account the PV power variations on a time basis. Hence, the power consumption from the battery is high and the change in voltage is also high. EMS between multiple MGs has been examined in (Wang et al., 2016a; Wang et al., 2016b; Rahbar et al., 2018). In this method, failure to consider the minimum and maximum ESS limits may render their results practically unenforceable. RES/load generation must have a stable process or precise distribution, which may not be possible for highly intermittent RES such as solar and wind. A coordinated control strategy for PV and ESSs is proposed in (Wu et al., 2015) considering the available power in RES and ESS SoC conditions. However, this algorithm requires additional control schemes to coordinate with the distributed MG elements connected on the AC bus side of the DC link to work. As a result, a wide range of power conditions from distributed RES and storage capacity from ESS must be considered globally to ensure that MGs are flexible and reliable. A power smoothing method for a large-scale PV plant is presented in (Wang et al., 2014). Due to the dynamic nature of modern MGs, it is impossible for the DC link voltage to be constant. The DC link voltage is affected by any power imbalance or fluctuation, and it is difficult to maintain the power balance and stability of the MG. ESS for renewable-grid integration of PV smoothing control is described in (Brahmendra Kumar et al., 2018). The batteries in this system must be able to handle any fluctuations in the DC link voltage due to changes in load or solar power generation. Consequently, the BS is subjected to high current stress, which shortens its lifetime.

Several important studies on this topic have been reported in the literature (Tummuru et al., 2015a; Tummuru et al., 2015b; Karimi et al., 2017; Manandhar et al., 2019; Xu et al., 2020; Hosseini et al., 2021; Jiang et al., 2021; Li et al., 2022). However, these studies have focused on isolated situations with DC link for RES-grid connected HESS or DG resources. Flexible operation of DC MG with HESS is proposed in (Tummuru et al., 2015a). However, more time is required for settling and computation in order to keep the DC link voltage stable. In (Hosseini et al., 2021), a unique EMS for grid-connected residential MG with ESS is proposed. However, the island operation of MG is not considered and is a very crucial part of the residential sector. In (Tummuru et al., 2015b; Manandhar et al., 2019), HESS and its EMS are described in detail. But this method can cause a drastic increase in battery charge and discharge rates produced during the transition, resulting in a decrease in battery life. These methods provide more settling time and the maximum overshoot is also higher. In MG management systems, a

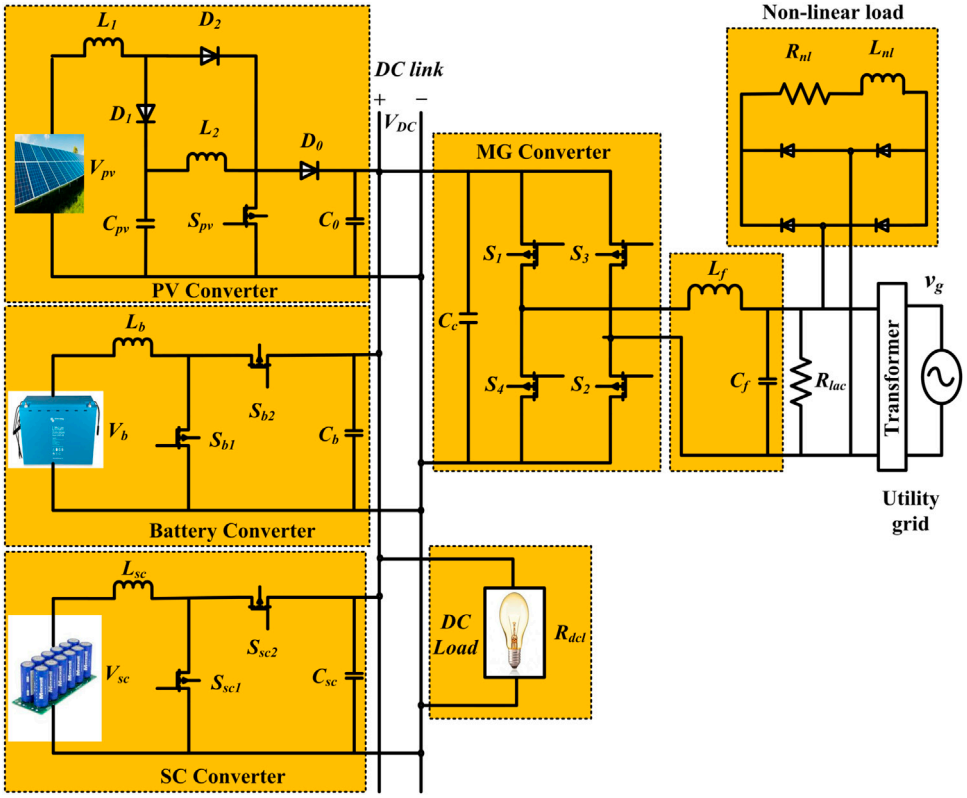

FIGURE 1
Proposed renewable-grid connected MG.

coordinated SoC control strategy is implemented to stabilize the bus frequency and voltage amplitude of MGs based on a model predictive control algorithm for DG and ESS units. If one communication link fails, the whole system is out of synchronization, so ESS and RES are coordinated by centralized management control (Li et al., 2022). According to the EMS proposed in (Xu et al., 2020), power can be injected or withdrawn from the grid based on changes in DC and AC load and changes in RES power. However, the grid operating conditions and charging conditions of the ESS are not taken into account. There is a dearth of details on off-MPPT and load shedding activities. In addition (Jiang et al., 2021), proposed an advanced control algorithm. Flexible demand sharing is considered in the proposed control strategy to achieve decentralized MG coordination, but more communication links and computational time are still required.

To avoid the use of external communication links, researchers have examined autonomous control methods for power distribution. For power management, AC/DC power lines have been proposed as communication channels (Karimi et al., 2017). Some high-frequency components are used in power line communication carriers to develop coordinated control strategies in (Alramlawi and Li, 2020), (Neto et al., 2018), but this introduces noise and the signal bandwidth must be designed carefully. Droop control regulates the output voltage and frequency of the DG unit to provide optimal active and reactive power sharing in AC MGs (Rosero et al., 2020). As a result, since most RES at MPP are controlled in power control mode (PCM), conventional droop methods for power management cannot be directly implemented in systems integrating RES and ESS. Furthermore, an adaptive droop control approach is proposed in (Li et al., 2021) for MGs operating in grid/isolated mode. This approach is based on the all-DG-droop approach, but the different core source conditions of the DG units are not taken into account.

The variable power generation and load demand are a challenge that can be efficiently and successfully addressed by a HESS that relies on BSs and SCs. The BS and SC lifespans can be greatly improved by avoiding overcharging and over discharging. In order to keep ESSs within their optimal performance range, prevent them from being damaged by overcharging or discharging. Hence, an efficient energy management system (EMS) is required. Based on the above shortcomings, a smoothing control based efficient EMS for MG with HESS is

proposed in this work. The primary objective of this study is to design and develop a RES-based MG system using RR control that can reduce power fluctuations and provide continuous power to the grid under different operational conditions with HESS. So, the EMS maintains the power balance in the MG and provides flexible and configurable control for various RES and load demand changes.

The main features of the proposed work are:

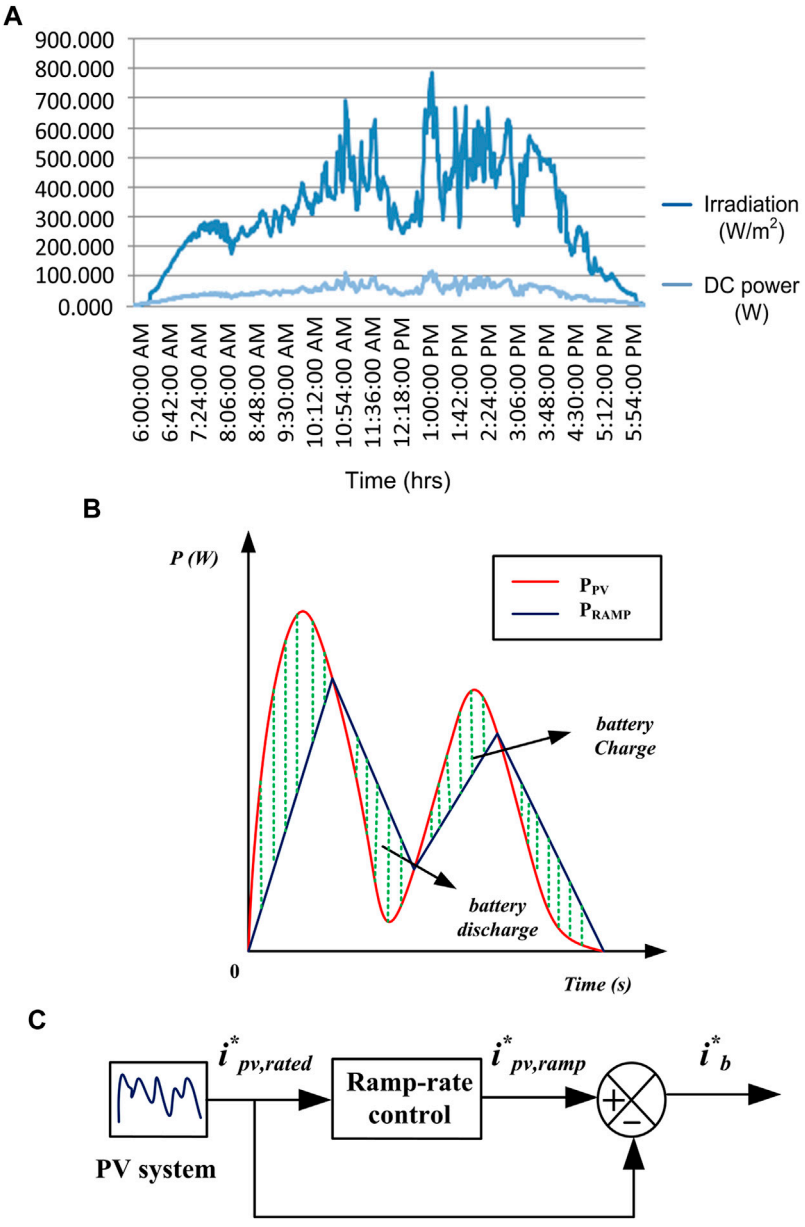

FIGURE 2
(A) Irradiation profile on a day (Kumar et al., 2020). **(B)** Battery power characteristics based on RR control (Kumar et al., 2020). **(C)** Ramp-rate control model diagram.

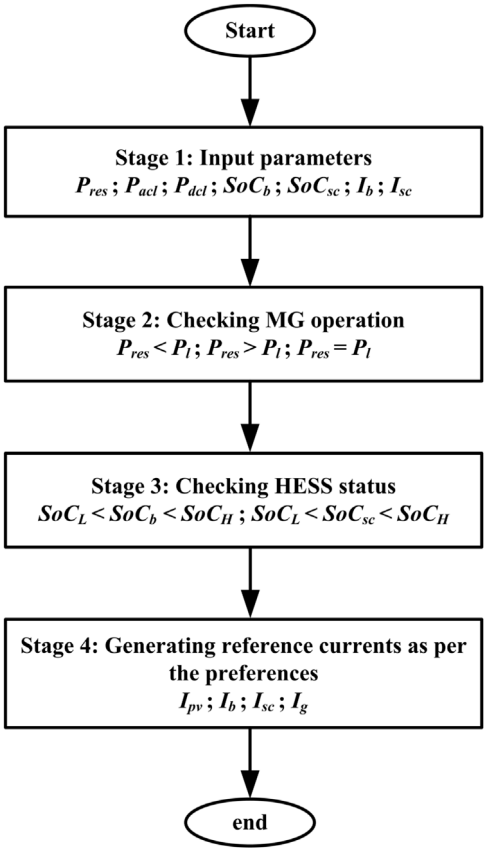

FIGURE 3
Control parameters for EMS.

i) PV power fluctuations are mitigated using RR control, which provides continuous operation of the system and improves system reliability.
ii) The obtained battery power is measured by limiting the PV power, which is the difference between the original PV power and the ramp-rate PV power by the RR controller. Therefore, the power consumption of the ESS depends upon the rise or fall rate of the PV power fluctuations.
iii) It limits the charge and discharge rates of the BS and SC.
iv) The recovery time of voltage is very low and achieves quick DC link voltage regulation.
v) reducing stress on the BS pack and increasing system life.
vi) Improvements in power quality at the PCC.
vii) Seamless power transfer between various grid and islanded connected modes and vice versa.

HIL prototyping can be used to test the proposed system in a real-time environment. An efficient renewable energy management system can be developed using this test bench to validate control algorithms in real time.

The organization of the paper is as follows: Section 2 describes the configuration and EMS of the proposed system. Section 3 discusses stability analysis and control of HESS. Section 4 presents the simulation results and discussion, and Section 5 explains the HIL implementation and results. Section 6 describes the conclusion.

2 Proposed system configuration and EMS

The renewable-grid connected MG with HESS is depicted in Figure 1. It comprises PV system with a single-stage inverter linked to the utility grid using a common DC-link. The BS and SC are connected to a common DC-link with two bidirectional buck-boost converters. During excess (EPM) or deficit mode (DPM), the BS provides or absorbs power, respectively. Surges in PV and

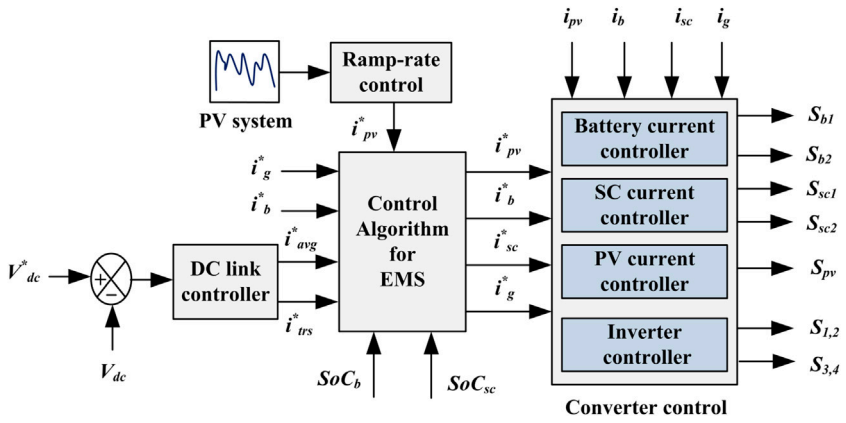

FIGURE 4
Simplified control of a proposed system.

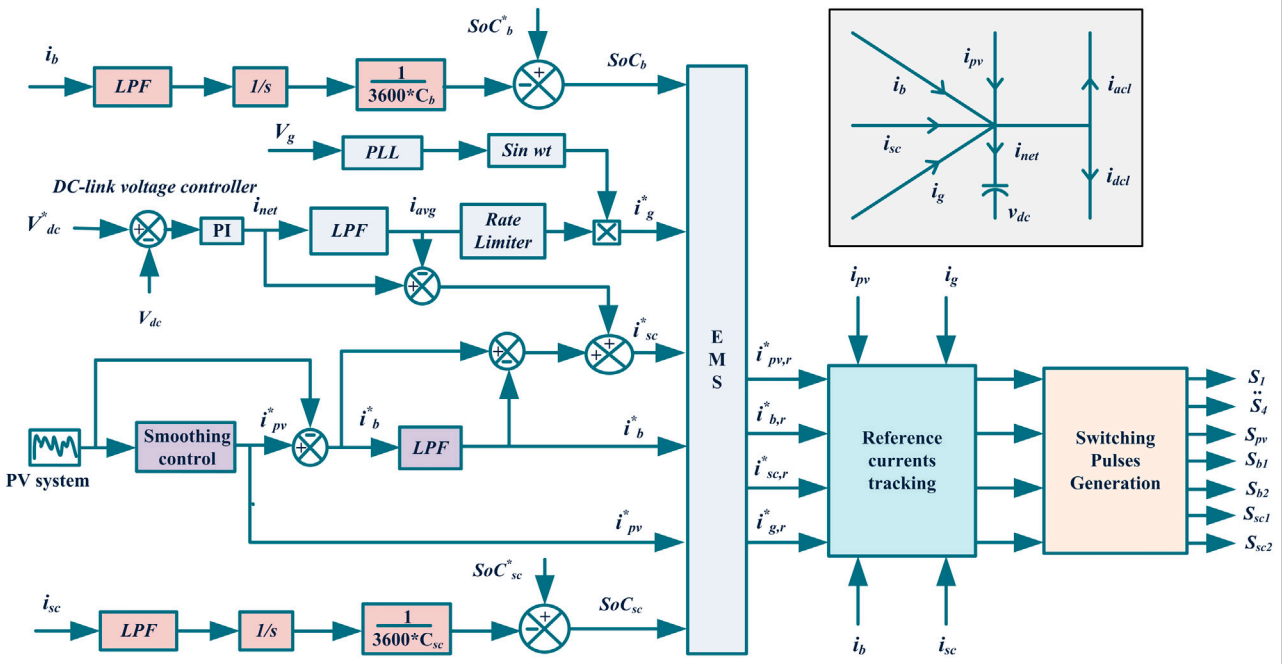

FIGURE 5
Overall proposed control system configuration.

load power are delivered/absorbed by SC. In addition, the SC unit reduces BS and grid stress by adjusting peak currents.

2.1 PV power analysis and ramp-rate control

The output of a PV system fluctuates significantly due to the irregular nature of solar energy due to climatic conditions. The maximum decrease/increase in PV generation on a cloudy or windy day is determined by the wind speed and the size of the PV plant. When clouds are moving quickly, PV output decreases significantly. Thus, the injection of PV energy into a distribution grid creates issues with power quality such as voltage variations, stability deprivation, *etc.* PV power variations are not severe under normal climate conditions, but severe climate conditions account for 70–90% of all PV power fluctuations (see Figure 2A). It is probable to alleviate these power quality issues by using an efficient ESS (Brahmendra Kumar et al., 2018). In order to smooth out the output of the PV, the BS can be used with RR control. The RR control is a method of limiting the rate of power change from the PV system in order to maintain grid stability. The battery power characteristics are presented in Figure 2B based on RR control. The area around the green line shows the minimum and maximum energy capacity of the battery that is needed to effectively smooth the variation in PV output.

Figure 2C Depicts a block diagram for a basic RR control system. The rate of rise/fall is limited to a maximum RR (r_{max}) value denoted as RES-RR. The maximum RR value that can be considered is 10%/min.

$$P_b^* = P_{pv,ramp}^* - P_{pv,rated}^* \tag{1}$$

The difference between rated PV power ($P_{pv,rated}^*$) and ramp-rate power ($P_{pv,ramp}^*$) generates the reference power for the battery (P_b^*). The sign of the generated power determines the charging and discharging conditions of the battery. If the sign is negative, the battery can be charged and *vice versa*. The $P_{pv,ramp}^*$ is calculated based on the maximum limit rate ($r_{\max}$). The required ramp-rate power ($P_{pv,ramp}^*$) equation is given below.

$$P_{pv,ramp}^{\star} = \frac{r_{max} \times P_{pv,rated}^{\star}}{60} \tag{2}$$

2.2 Converters control of the proposed system

As illustrated in Figure 3, the EMS control parameters balances power between RES, grid and ESS. This algorithm takes into account the present state of P_{pv}, P_l, SoC_b, SoC_{sc}, I_b, and I_{sc} as input parameters. The algorithm starts with input parameters and secondly, the algorithm considers these variables to decide the operation mode of MG (i.e., RES balances or less or more than the

TABLE 1 A DPM. B EPM.

Modes	DPM
$SoC_b > L_b$ and $SoC_{sc} > L_{sc}$	$i^*_b = \rho i_{avg}$, $i^*_{sc} = i_{sc,r}$, $i_g = (1-\rho)\, i_{avg}$
$SoC_b < L_b$ and $SoC_{sc} > L_{sc}$	$i^*_b = 0$, $i^*_{sc} = i_{sc,r}$, $i_g = i_{avg}$
$SoC_b > L_b$ and $SoC_{sc} < L_{sc}$	$i^*_b = \rho i_{avg}$, $i^*_{sc} = 0$, $i_g = (1-\rho)\, i_{avg} + i_{sc,r}$
$SoC_b < L_b$ and $SoC_{sc} < L_{sc}$	$i^*_b = 0$, $i^*_{sc} = 0$, $i_g = i_{avg} + i_{sc,r}$
Modes	**EPM**
$SoC_b < H_b$ and $SoC_{sc} < H_{sc}$	$i^*_b = -i_{b,r}$, $i^*_{sc} = -i_{sc,\ ra} + i_{sc,r}$, $i_g = i_{net}$
$SoC_b > H_b$ and $SoC_{sc} < H_{sc}$	$i^*_b = 0$, $i^*_{sc} = -i_{sc,\ ra} + i_{sc,r}$, $i_g = i_{net}$
$SoC_b < H_b$ and $SoC_{sc} > H_{sc}$	$i^*_b = -i_{b,ra}$, $i^*_{sc} = 0$, $i_g = i_{net} + i_{sc,r}$
$SoC_b > H_b$ and $SoC_{sc} > H_{sc}$	$i^*_b = 0$, $i^*_{sc} = i_{sc,r}$ *or* 0, $i_g = i_{net} + i_{sc,r}$

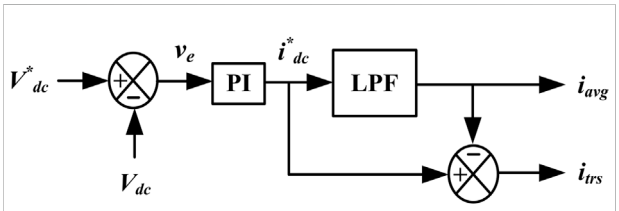

FIGURE 6
DC-link voltage controller.

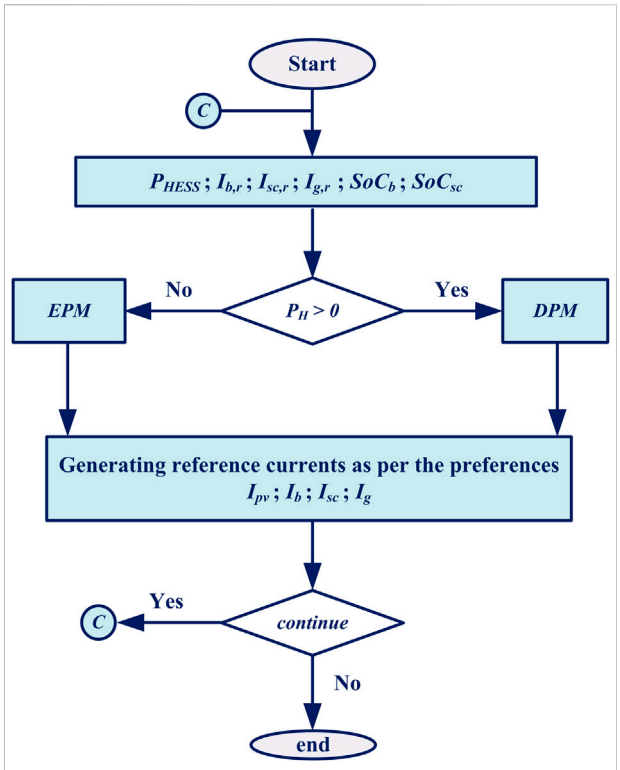

FIGURE 7
Conditions of the proposed EMS.

load demand). The BS and SC status of SoCs is analyzed in the third stage, i.e., whether SoC_b and SoC_{sc} are within or above the SoC_H or SoC_L limits. Finally, different BS and SC reference conditions and preferences are determined by various grid-interactive states that decide the MG-VSC reference, such as grid sharing, grid injection or idle mode, and also by BS and SC charging and discharging, or both charging and discharging, or both being in idle conditions. By limiting SoC_b and SoC_{sc} to safe levels, this technique considers the ESS's energy content and limits active involvement to its rating.

The EMS and converter control are shown in Figure 4 as a simplified control scheme for this proposed system. The reference currents for the BS, SC, and MG-VSC converters are generated according to the scheme shown in Figure 5. To generate the error signal, a comparison is made between the actual (i.e., i_{pv}, i_b, i_{sc}, i_g) and reference currents in the current controller. The BS, SC, and RES-based converters rely on the modular signals generated by PI controllers for input. A hysteresis current controller regulates the MG-VSC's switching pulses.

2.3 Generation of reference currents

A constant DC-link voltage maintains system power balance (Neto et al., 2018). A DC-link controller generates a net current (i^*_{dc}) that is either injected or drawn from the DC-link. A PI controller processes this signal to generate the net current (i^*_{dc}), which is shown in Figure 6. The voltage control loop written in (4) is used to calculate the total current, $i_{net}(t)$. The HESS and the utility grid must sustain power balance by dividing the i_{net} into average (i_{avg}) and transient (i_{trs}) components, respectively.

$$v_e(t) = v^*_{dc}(t) - v_{dc}(t) \tag{3}$$

$$i_{net}(t) = k_p v_e(t) + k_i \int v_e(t) \tag{4}$$

$$i^*_{avg}(t) = \left(\frac{1}{1 + s\tau_c}\right) i_{net}(t) \tag{5}$$

$$i^*_{trs}(t) = \left(1 - \frac{1}{1 + s\tau_c}\right) i_{net}(t) \tag{6}$$

The DC-link power (P_{dc}) is taken by,

$$P_{dc}(t) = v^*_{dc}(t) i_{avg}(t) \tag{7}$$

Where k_p and k_i are the PI controller's proportional and integral components, and τ_c is the low-pass filter time constant. The control structure and power balance at the DC-link are illustrated in Figure 5 and the equation is as follows:

$$P_{pv}(t) \pm P_{hess}(t) \pm P_g(t) = P_{dcl}(t) + P_{acl}(t) \tag{8}$$

Where P_{pv}, P_g, P_{hess}, P_{dcl}, and P_{acl} are PV, grid, HESS, DC and AC load powers, respectively.

TABLE 2 Charge/discharge coefficient (ρ).

Modes	$SoC_b(t)$	ρ	1-ρ
State-I	$0.9 < SoC_b < H$	1	0
State-II	$0.5 < SoC_b < 0.9$	0.7	0.3
State-III	$0.1 < SoC_b < 0.5$	0.3	0.7
State-IV	$SoC_b < L$	0	1

TABLE 3 System parameters.

Parameters	Values
PV system @ STC: PV voltage (V_{pv})	40 V
PV current (I_{pv})	20 A
BS pack: Ah capacity	14 Ah
Terminal voltage (V_b)	12 V
No. of batteries in series	4
BS converter: L_b, C_b	5 mH, 220 μF
SC pack: Terminal voltage (V_{sc})	16.2 V
Rated capacitance (C_{sc})	58 F
Maximum peak current (I_p)	200 A
Maximum continuous current (I_{mc})	19.3 A
SC converter: L_s, C_s	5 mH, 220 μF
PV converter: L_1, L_2, C_{pv}, C_0	5 mH, 2mH, 110 μF, 220 μF
VSC: L_f, C_f, C_c	5 mH, 15 μF, 1,000 μF
AC load and DC load: R_{Lac}, R_{Ldc}	50 Ω, 25 Ω
1-Φ Bridge rectifier: R_{nl}, L_{nl}	20 Ω, 1 mH
Utility grid and DC-grid: V_g, f	230 V, 50 Hz
V_{dc}	80 V

2.4 Proposed EMS

It operates in two modes: 1) excess power (EPM: $P_H > 0$) and (ii) deficit power (DPM: $P_H \leq 0$) modes. Two operating modes are considered depending on the availability of RES power generation and system load requirements. The balance equation for EPM and DPM is $P_H = P_b + P_{sc} + P_g = P_{dcl} + P_{acl} - P_{pv}$. As illustrated in flowchart Figure 7, the system works in various modes of operation depending on the condition of P_H. As shown in Tables 1A,B, DPM and EPM distinguish four distinct operating modes based on the conditions of the SoC_b and the SoC_{sc}.

An important part of BS-based devices is the State of charge (SoC), which also improves BS performance. The BS can be protected, overcharging can be prevented, its lifetime can be extended, and the system's accuracy can be improved with proper SoC calculations (Hosseini et al., 2021). The SoC of BS and SC is calculated using the count-coulomb approach and the resulting equations are given by,

$$SoC_b = SoC_{bin} - \frac{1}{3600C_{Nb}} \int i_b dt \tag{9}$$

$$SoC_{sc} = SoC_{scin} - \frac{1}{3600C_{Nsc}} \int i_{sc} dt \tag{10}$$

The current $i(t)$ is measured and integrated over time to calculate the amount of energy that remains in the battery and SC. SoC helps to analyse battery and SC whether to charge or stop charging. This approach relies on exact measurements of battery and SC current and initial SoC. Where SoC_{bin} and SoC_{scin} are the BS and SC initial SoCs, C_{Nb}, and C_{Nsc} are the BS and SC nominal capacitances, and i_b and i_{sc} are the BS and SC currents.

The operational objectives defined for DPM are discussed in the following sections.

State I: Discharging both the BS and SC is necessary if $SOC_b > L_b$ and $SOC_{sc} > L_{sc}$. The BS, SC, and grid settings are set to the following,

$$i_b^* = \rho.i_{avg}^*,\ i_{sc}^* = i_{sc,r}^*,\ i_g^* = (1-\rho).i_{avg} \tag{11}$$

ρ represents the charging and discharging condition of the BS. Table 2 contains the results of a four-state logic used to determine the value of ρ.

State II: The BS should be idle if $SoC_b < L_b$ and $SoC_{sc} > L_{sc}$. SC provides transient and oscillatory current while the grid meets average power demand.

$$i_b^* = 0,\ i_{sc}^* = i_{sc,r}^*,\ i_g^* = i_{avg} \tag{12}$$

State III: The SC should be idle if $SoC_b > L_b$ and $SoC_{sc} < L_{sc}$, and the BS is discharged until SoC_b reached L_b to meet the average power demand while the SC is idle or charged from the grid. The grid supplies the required SC and average power demand.

$$i_b^* = \rho.i_{avg}^*,\ i_{sc}^* = 0,\ i_g^* = (1-\rho).i_{avg} + i_{sc,r} \tag{13}$$

State IV: When $SOC_b < L_b$ and $SOC_{sc} < L_{sc}$, the BS and SC are idle or charged by the utility grid. The grid is able to handle the total difference between generation and load power requirements.

$$i_b^* = 0,\ i_{sc}^* = 0,\ i_g^* = i_{avg} + i_{sc,r} \tag{14}$$

In this case, the grid supplies both average and transient power demand.

3 Stability analysis and controller design for HESS

As the charge/discharge cycles of the SC are much faster than the battery, the PI controllers are adjusted to the corresponding SC power stage. When using SC, the BW of the inner CCL is set at $f_{sw}/6$. The BW of battery is kept lower than SC current loop BW ($f_{sw}/10$) to redirect the fast-changing transient to the SC (Kollimalla et al., 2014). The gain H is considered to be one

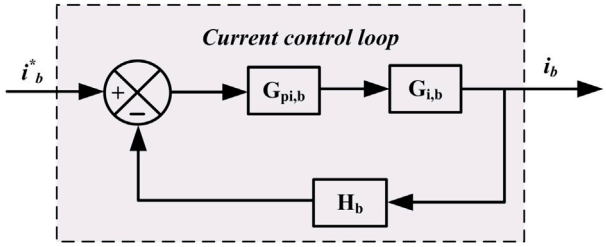

FIGURE 8
Battery CCL block diagram.

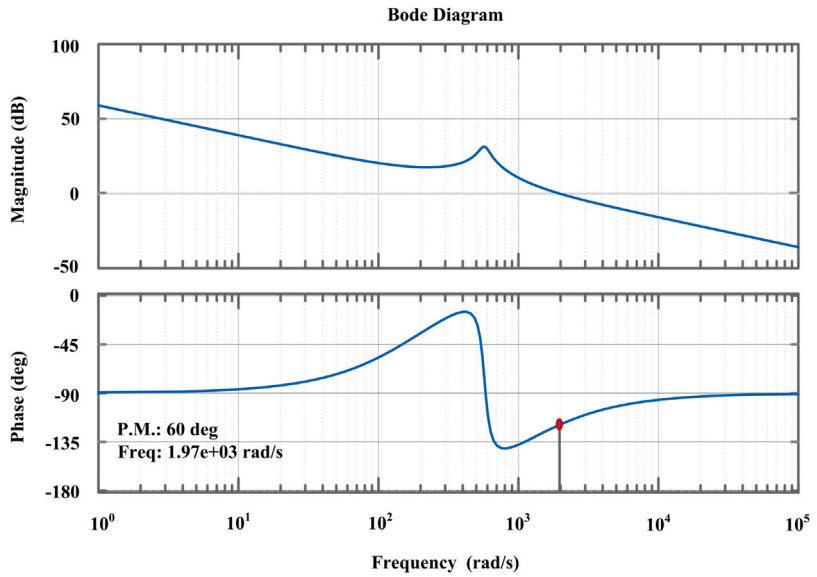

FIGURE 9
Bode plot of CCL for battery.

for all converters. Table 3 lists the variables for the converters considered in the calculation part of the equations below.

3.1 Design of battery current control loop

The battery controller block diagram is presented in Figure 8. The TF of control to inductor current is taken as (Kollimalla et al., 2014),

$$G_{i,b} = \frac{V_0 C_b s + 2\frac{V_0}{R_L}}{L_b C_b s^2 + \frac{L_b}{R_L} s + (1 - D_b)^2} \tag{15}$$

The TF of CCL compensator is as follows:

$$G_{pi,b} = K_{p_b} + \frac{K_{ib}}{s} \tag{16}$$

The OLTF of CCL is given by,

$$G_{OL,b} = G_{pi,b} G_{i,b} H_b \tag{17}$$

The Bode plot of the OLTF for the battery is depicted in Figure 9. To develop and optimize the control parameters, the SISO tool is used. The PI controller is calibrated to obtain a PM of 60° at rate of 1.97 krad/s. The calculated D_b, K_{pb} and K_{ib} parameters are 0.4, 0.1 and 11, respectively.

3.2 Design of SC current control loop

The SC controller block diagram is presented in Figure 10. The TF of control to inductor current is taken as (Kollimalla et al., 2014),

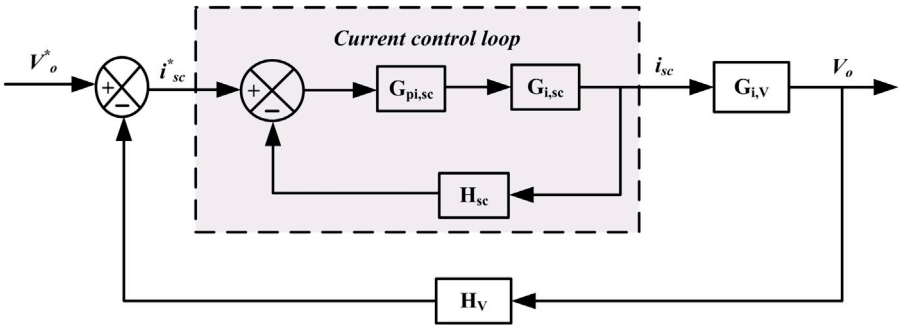

FIGURE 10
SC CCL block diagram.

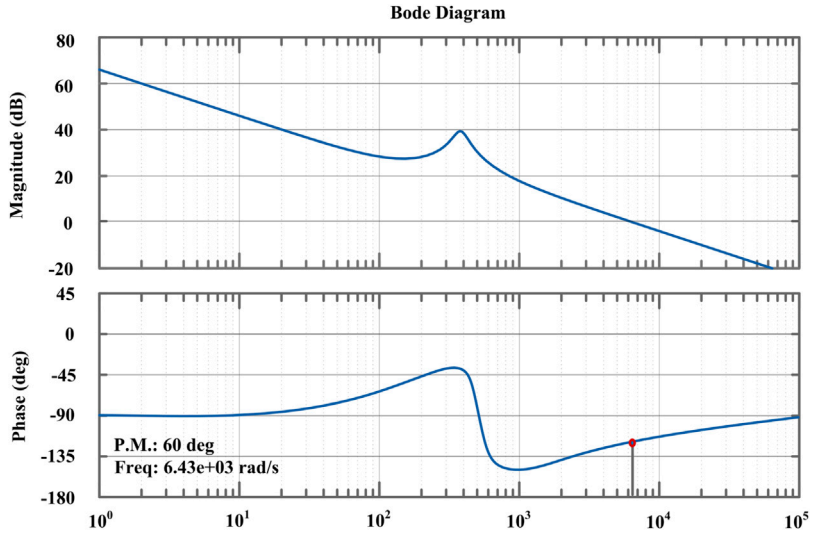

FIGURE 11
Bode plot of CCL for SC.

$$G_{i,sc} = \frac{V_0 C_s s + 2\frac{V_0}{R_L}}{L_s C_s s^2 + \frac{L_s}{R_L} s + (1 - D_{sc})^2} \tag{18}$$

The TF of CCL compensator is as follows:

$$G_{pi,sc} = K_{p_{sc}} + \frac{K_{isc}}{s} \tag{19}$$

The OLTF of CCL is given by,

$$G_{OL,sc} = G_{pi,sc} G_{i,sc} H_{sc} \tag{20}$$

The Bode plot of OLTF for SC is depicted in Figure 11. The PI controller is calibrated to obtain a PM of 60° at rate of 6.43 krad/s. The calculated D_s, K_{psc} and K_{isc} parameters are 0.6, 0.56 and 120, respectively.

3.3 Design of voltage control loop for HESS

The TF of VCL is taken as (Kollimalla et al., 2014),

$$G_{i,V} = \frac{R_L (1 - D_s)\left(1 - \frac{L_s}{R_L (1-D_s)^2 s}\right)}{2 + RC_s s} \tag{21}$$

The TF of VCL compensator is as follows:

$$G_{pi,V} = K_{p_V} + \frac{K_{iV}}{s} \tag{22}$$

The OLTF of VCL is given by,

$$G_{CL,sc} = \frac{G_{pi,sc} G_{i,sc}}{1 + G_{pi,sc} G_{i,sc} H_{sc}} \tag{23}$$

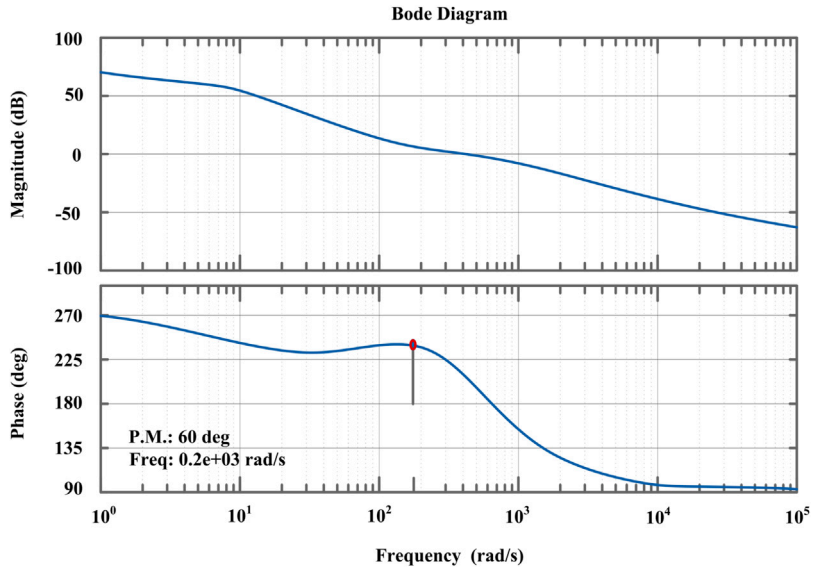

FIGURE 12
Bode plot of VCL for HESS.

$$G_{OL,sc} = G_{pi,V} G_{CL,sc} G_{i,V} H_V \tag{24}$$

The Bode plot of the OLTF for the voltage controller is depicted in Figure 12. The PI controller is calibrated to obtain a PM of 60° at rate of 0.2 krad/s. The calculated D_s, K_{pV} and K_{iV} parameters are 0.6, 0.23 and 15, respectively.

4 Simulation results

The MATLAB/Simulink environment has been used to test the validity of the proposed system. Table 3 lists the proposed system parameters. According to the SoC status ESS in Figure 13 and Figure 14, four different operating modes are shown in this section.

Under DPM, this power mode has four defined states of operation modes based on the SoC status of the ESDs.

State-1 ($SoC_b > L$ and $SoC_{sc} > L$): In Figure 14, the BS and grid power share the deficit load power ($P_{deficit}$) up to $SoC_b < L$. At $t = 1s$, the SC pack produces an instant variation in the P_{dcl}. This state provides quick DC-link voltage control and smooth operation of the BS, as shown in Figure 13A and Figure 13C.

State-2 ($SoC_b < L$ and $SoC_{sc} > L$): The P_b reference is set to zero in Figure 14. Thus, the grid provides the entire deficit power under a steady-state condition, while SC removes the sudden

TABLE 4 Proposed EMS power changes in various operation modes.

Modes of operation	DPM							EPM		DPM					
Time ranges	t_0	t_1	t_2	t_3	t_4	t_5	t_6	t_7	t_8	t_9	t_{10}	t_{11}	t_{12}	t_{13}	t_{14}
PV Power (W)	100	100	100	180	180	260	260	360	360	270	270	120	160	160	80
SoC_b	>L	>L	>L	>L	>L	>L	>L	<H	<H	<L	>L	>L	>L	>L	>L
SoC_{sc}	>L	>L	>L	>L	>L	>L	>L	<H	<H	>L	>L	>L	<L	>L	>L
BS Mode	DM	DM	DM	DM	DM	DM	DM	CM	DM	Idle	DM	DM	DM	DM	DM
SC Mode	CM	DM	DM	CM	DM	CM	DM	CM	CM	DM	CM	DM	Idle	CM	DM
Grid Mode	SL	SL	SL	SL	SL	SL	SL	CG	SL	SL	SL	SL	SL	SL	SL
Load Power (W)	130	263	263	263	263	270	270	270	285	270	275	270	270	270	270

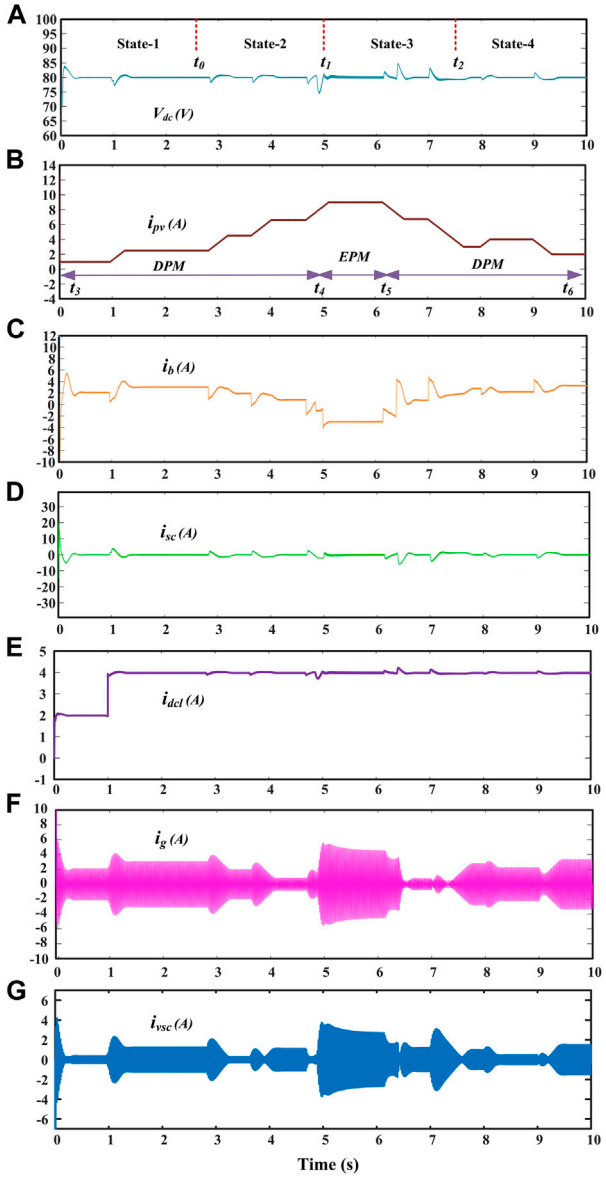

FIGURE 13
(A) DC-bus voltage, **(B)** PV, **(C)** BS, **(D)** SC, **(E)** DC load, **(F)** grid, and **(G)** VSC currents.

power variations at $t = t_0$. In Figure 13G, i_{vsc} achieves a smooth transition.

State-3 ($SoC_b > L$ and $SoC_{sc} < L$): At $t = t_1$, the BS and grid share the $P_{deficit}$ until $SoC_b < L$, as depicted in Figure 14.

State-4 ($SoC_b < L$ and $SoC_{sc} < L$): At $t = t_2$, total $P_{deficit}$ is provided by the utility grid. Figure 13A shows the DC-link voltage, whereas Figures 13C-G show the respective changes in BS, SC, DC load, grid and VSC currents.

Under EPM: This mode charges the ESDs with extra power from RES until it reaches its maximum SoC limits. The VSC then supplies additional power to the grid. The various power outcomes of the system are illustrated in Figure 14.

Figure 13B shows the PV current profile under different operating modes, as the system transitions from one mode to another depending on the available RES and load power circumstances. During abrupt variations in PV and/or load, the SC provide/absorb transient power. The i_{pv} is generated at t_3-t_4 instants lower than the load requirement. So, the system works in DPM mode with the BS and the utility grid sharing the $P_{deficit}$. During t_4-t_5, i_{pv} exceeds the load demand. This results in

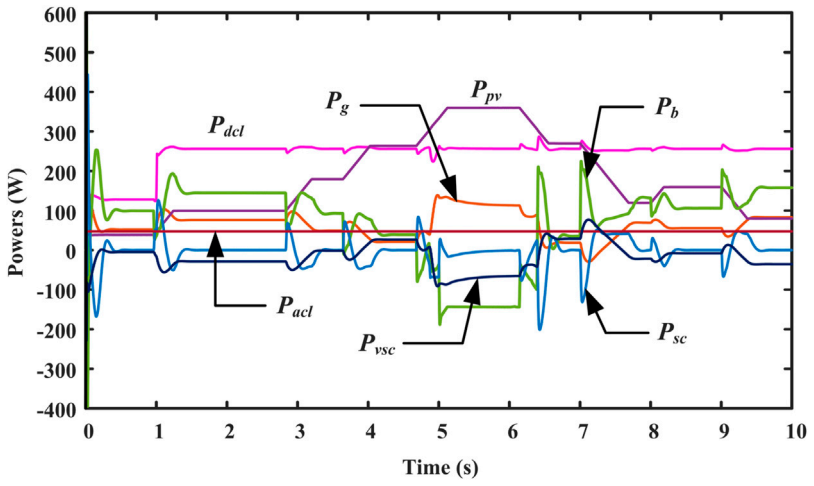

FIGURE 14
Various power results.

the system running in EPM mode, with the excess power mainly used to recharge the ESSs. In the t_5-t_6 instants, i_{pv} is once again below the load requirement. Thus, the system works in DPM. Smooth changes in i_b, i_g and i_{vsc} are seen during the transition phase, as shown in Figure 13C, Figure 13F,G.

The i_{vsc} is depicted in Figures 15A as the DC load varies. At $t = 1s$, the i_{dc} has increased, and the VSC uses grid power to supply the increased DC demand. Figures 15B–D depict the power quality characteristics of the proposed system. The non-linearity in AC load increases at $t = 9s$ in Figure 15B and the VSC provides harmonic elements for the load, as illustrated in Figure 15C. Therefore, unity power factor (UPF) can be achieved on the grid as a result of stable i_g, as illustrated in Figure 15D. Harmonic and reactive load current elements are supplied by MG-VSC in this system to run the utility system at UPF.

5 HIL implementation

The OP5700 HIL testbed setup is used to validate the proposed system as shown in Figure 16. In HIL setup, RT-LAB, PCB-E06-0560, LAN network, MSOX3014T probes, and connecting wires are all used. Analog outputs and digital inputs on the PCB can be utilized to exchange data between the simulation and real controller. The proposed EMS operates in various power modes depending on the P_H value. Figure 13 illustrates the ESS, grid currents, and DC link voltage when P_H is less than zero (DPM) and greater than zero (EPM). In each power mode, the states of the ESSs change in accordance with the respective SoCs.

5.1 Performance under EPM operation

The scale of the figures presented in Figures 17, 18, 19, the *X*-axis represents the time per division (s/div) and the *Y*-axis represents the current (A/div), voltage (V/div), and power (W/div) values per division. Figures 17A–H illustrates the performance of the EMS during EPM operation. In this mode, the generation exceeds load demand by a predetermined margin.

The PV current profile shown in Figure 17Aa. The response battery and SC current profiles are presented in Figure 17Ab,c. At time t_1, SoC_b and SoC_{sc} are lower than H. Changes are made to the DC load at time $t_1 = 1s$ in Figure 17Bb, which results in a voltage deviation in the DC link. In this state, charge the BS and SC to their rated charging capacity and the SoC will attain its maximum value. The grid provides the required P_{avg} to sustain a stable DC link voltage in Figure 17Ba. The SC device provides transient power.

When SoC_b reaches H_b at time t_2, i_b equals zero. The SC is charged at its rated current in this state because the SoC_{sc} is still less than the H_{sc}. The SC is charged with a part of the surplus power, and the remaining surplus power being fed back into the grid.

At time t_3, when SoC_{sc} reaches H_{sc}, i_{sc} equals zero. After that, the BS is charged at its rated current until H_b is reached. The grid utilizes both transient and average power to sustain a stable DC link voltage during this condition in Figure 17Ba.

The At time t_4, i_{acl} has increased in Figure 17Ca. At this point, SoC_{sc} is equal to H_{sc} and SoC_b is lower than H_b. As a result, the charging current i_b is constant and the transient power is delivered by the SC. The response of grid and VSC currents is illustrated in Figures 17Cb,c.

At time t_5, SOC_b and SOC_{sc} are higher than H. In this state, the grid is able to stabilize the DC link voltage. The generation meets the total demand and surplus power is fed back into the grid. The i_g and

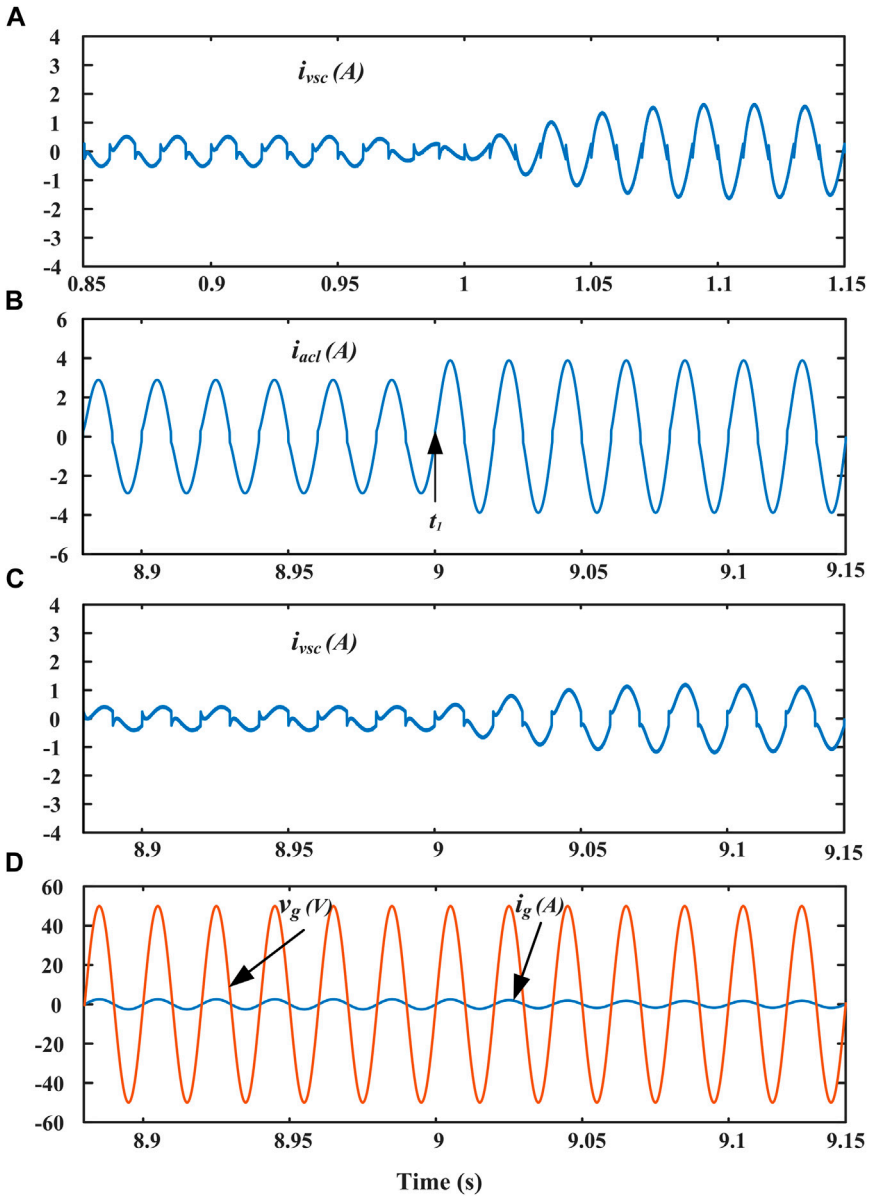

FIGURE 15
Features of power quality of the proposed system.

v_g operate at unity power factor under all operating conditions. Figures 17D–G show the constant AC load, VSC, grid currents and various power results of PV, BS, SC, VSC, grid, DC and AC loads. Figures 17Ha-c show the inverter, AC load, grid currents, and grid voltage, respectively.

5.2 Performance under DPM operation

In this case, the i_{pv} is less than the load demand, resulting in a $P_H < 0$ and the PV current profile shown in Figure 18Aa remains constant. The SOC_b and SOC_{sc} thresholds are changed to observe the system behavior under extreme conditions. Hence, the controller and the proposed EMS can be studied under extreme operating circumstances.

Condition I: The $P_{deficit}$ shared by BS with the grid power until $SoC_b < L$. The DC load is being changed from R = 50Ω–25 Ω at t_1 in Figure 18Bb. As i_b increases slowly in Figure 18Ab, the SC adjusts to the rapidly changing DC load power depicted in Figure 18Ac. Therefore, V_{dc} is quickly regulated in Figure 18Ba and i_b changes smoothly as shown in Figure 18Ab.

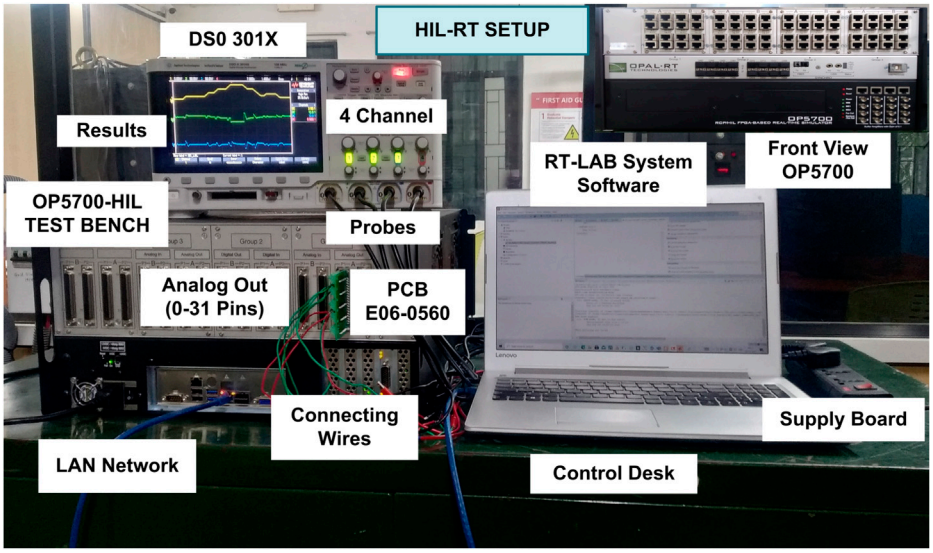

FIGURE 16
HIL experimental testbed.

Condition II: In this case, the SOC_b is reduced. As a result, the grid supply deals with the active power demand under steady state, where the SC pack absorbs a transient change in power at $t = t_2$. Therefore, i_{vsc} achieves a smooth change at instant t_2 in Figure 18Cb. The grid current response is shown in Figure 18Cc.

Condition III: SOC_b is greater than L_b and SOC_{sc} is less than L_{sc}. The BS and grid supply handle the deficit load power until $SoC_b < L$.

Condition IV: Both SoC_b and SoC_{sc} are low in this condition. As a result, the grid provides the necessary power to sustain the V_{dc} at a stable level. In Figure 18Ca, the AC load increases at times t_2 and t_3. The SoC_{sc} is now lower than L_{sc}. As a result, i_{sc} becomes zero. The i_b gradually rises as the grid contributes to compensating the $P_{deficit}$ in the system and SC provides the transient change in power. Figures 18D–G show the constant AC load, grid, VSC currents and various power results of PV, BS, SC, VSC, grid, DC and AC loads. show the various power results of PV, BS, SC, VSC, grid, DC, and AC loads. Figure 18H shows the grid current and voltage, which are sinusoidal in nature.

5.3 Performance under various operation modes

Figure 19A depicts the proposed EMS dynamic performance in various operating modes based on variations in RES power. Figure 19Aa illustrates the high-gain RES converter with emulated RES current pattern applied to determine the feasibility of the proposed scheme. The i_{pv} reduces the load demand between instants t_0 and t_7. Hence, the system works in DPM, sharing the available power between the BS and the utility grid. During the t_7 and t_8 instants, i_{pv} exceeded the load demand. So, the system operates on EPM, and ESDs are charged with surplus power. Again, the i_{pv} is lower than the load demand ranges from t_8 to t_{15}. Thus, the system runs on DPM as shown in Figure 19A. The smooth changes in i_b, i_g, and i_{vsc} that occur during the mode transition are depicted in Figures 19Ab,Cb,Cc.

The power sharing between the seamless transfer operation modes is summarized in Table 4. Where CM: charging mode, DM: discharging mode, CG: charging from the grid, SL: load sharing, respectively. The results show that the high-power-density SC pack and its effective control of the DC link

TABLE 5 Comparative analysis of the proposed system with existing methods.

Parameters index	Sathishkumar et al. (2012)	Manandhar et al. (2019)	Tummuru et al. (2015b)	Proposed method
M_p (%)	5	5.3	3.4	3.1
T_r	900 ms	650 ms	440 ms	230 ms
Grid current (I_g) THD	5.3%	4.2%	<7%	2.14%

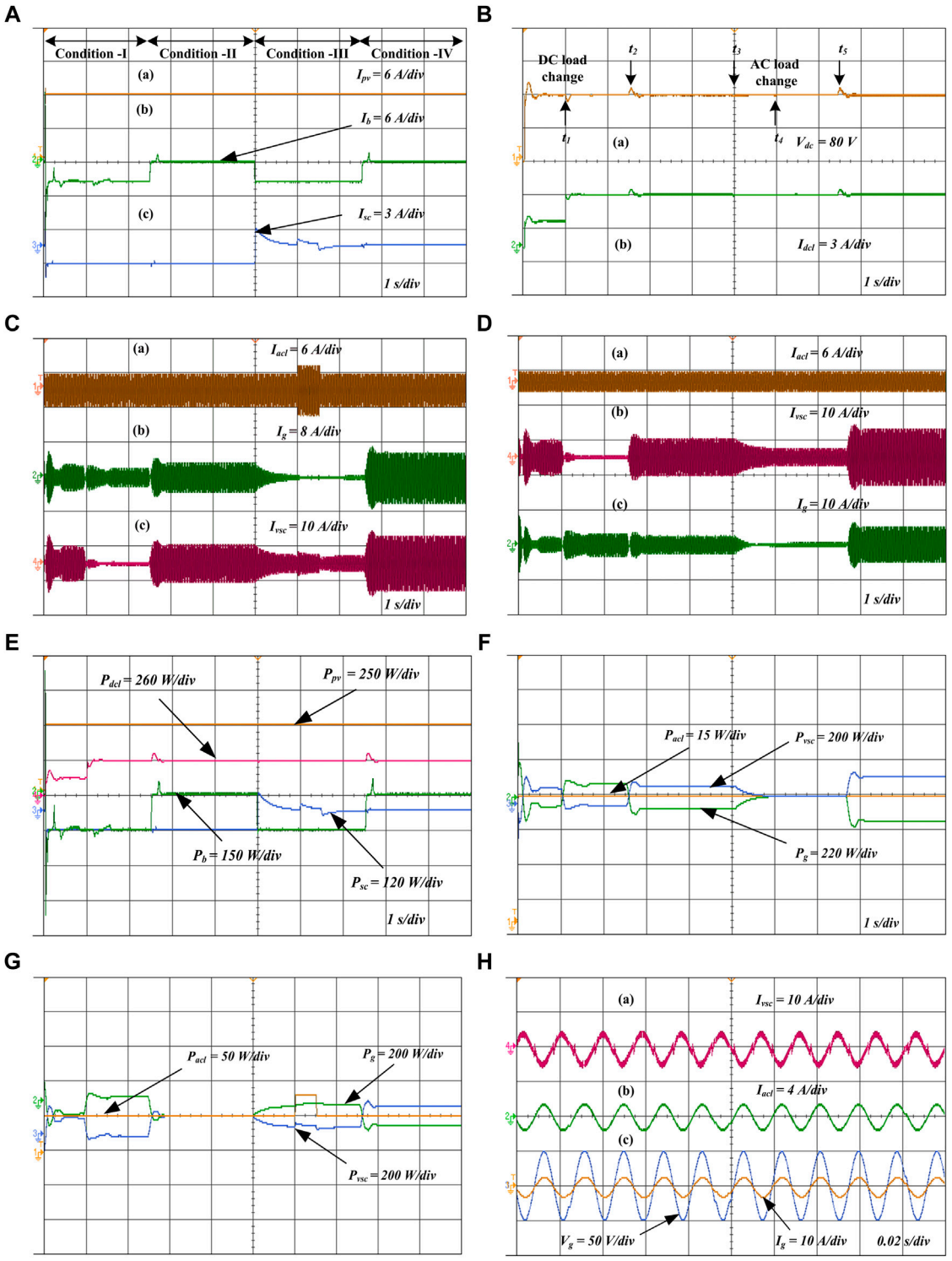

FIGURE 17
(A) HIL results: (a) PV, (b) BS, and (c) SC currents. **(B)** HIL results: (a) DC-link voltage, (b) DC load current. **(C)** HIL results: (a) AC load, (b) grid, and (c) VSC currents. **(D)** HIL results: (a) constant AC load, (b) VSC, and (c) grid currents. **(E)** HIL power results for PV, BS, SC, and DC load under EPM operation. **(F)** HIL power results for VSC, constant AC load and grid. **(G)** HIL power results for VSC, AC load, and grid. **(H)** HIL results: (a) VSC current, (b) AC load current, (c) grid current and voltage.

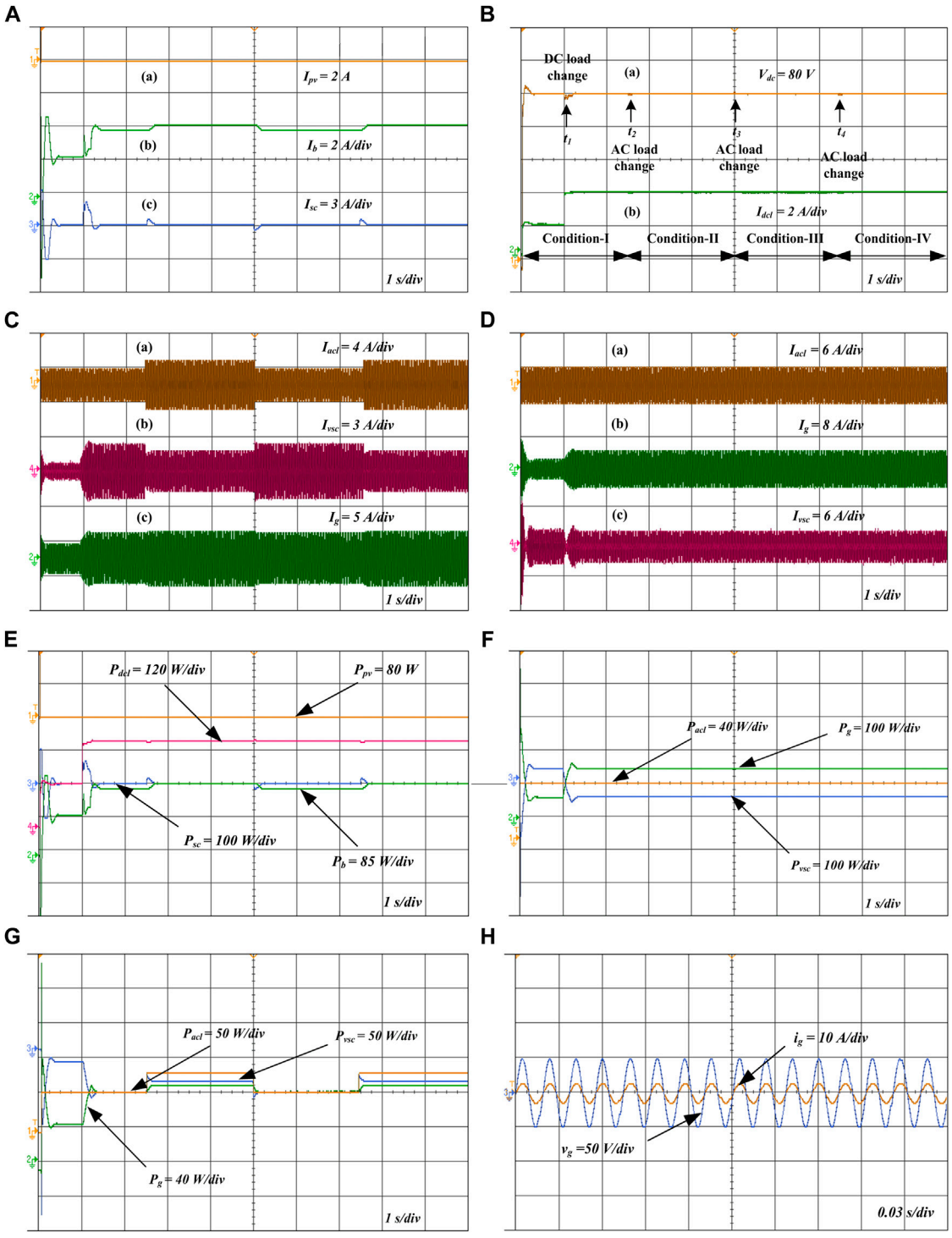

FIGURE 18
(A) HIL results: (a) PV, (b) BS, and (c) SC currents. **(B)** HIL results**:** (a) DC-link voltage, (b) D**C** load current. **(C)** HIL results: (a) AC load, (b) VSC, and (c) grid currents. **(D)** HIL results: (a) constant AC load, (b) grid, and (c) VSC currents. **(E)** HIL power results for PV, BS, SC, and DC load under DPM operation. **(F)** HIL power results for VSC, constant AC load and grid. **(G)** HIL power results for VSC, AC load and grid. **(H)** HIL results: grid current and grid voltage.

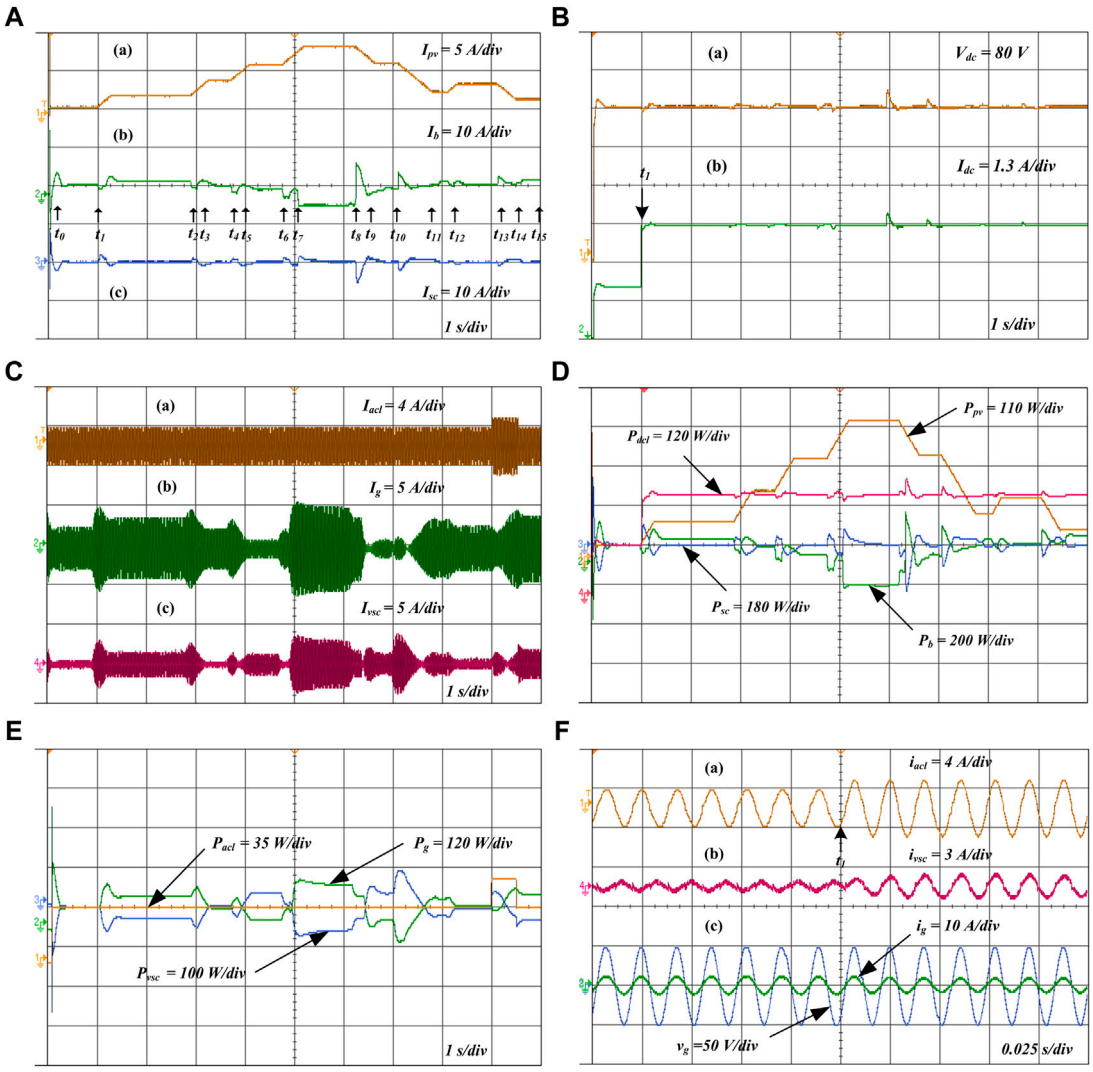

FIGURE 19
(A) HIL results: (a) PV, (c) BS, and (c) SC currents. **(B)** HIL results: (a) DC-link voltage, (b) DC load current. **(C)** HIL results: (a) AC load, (b) grid, and (c) VSC currents. **(D)** HIL power results for PV, BS, SC, and DC load under seamless mode of operation. **(E)** HIL power results for VSC, AC load, and grid. **(F)** (a) AC load current, (b) VSC current, and (c) grid current and grid voltage.

voltage significantly reduce the dynamics of the DC link voltage. The BS lifespan can be extended due to the reduced current stress due to reduced DC link voltage dynamics with the proposed EMS.

As the DC load varies at t_1 in Figure 19Bb, the PV generation also varies as illustrated in Figure 19Aa. At time t_1, BS switches from a -1.2 A charging mode to +2.2 A discharging mode in response to varying load demand as shown in Figure 19Ab. As depicted in Figure 19Ac, the SC absorbs the transient power generated by the load and PV variation during the step change in load demand, thereby reducing BS stress. The i_b gradually increases to compensate for the loss of low-frequency power. Hence, the BS endures less stress and the DC grid remains stable in Figure 19Ba. As can be seen in Figures 19D,E, the system dynamically switches between modes in response to the availability of RES power and current load conditions. The SC packs supply/absorb the transient power surges caused by rapid variations in RES and/or load, and the surplus average power generated in the DC link is utilised to charge ESDs or to inject into the utility grid, depending on the SoC of ESDs. The proposed EMS power quality features are illustrated in Figure 19F for various operating modes. When the VSC is not connected, i_g has both fundamental and harmonic load current components. The nonlinear component of the AC load increases at t_1 in Figure 19Ca and Figure 19Fa. A DC-AC inverter compensates for the non-

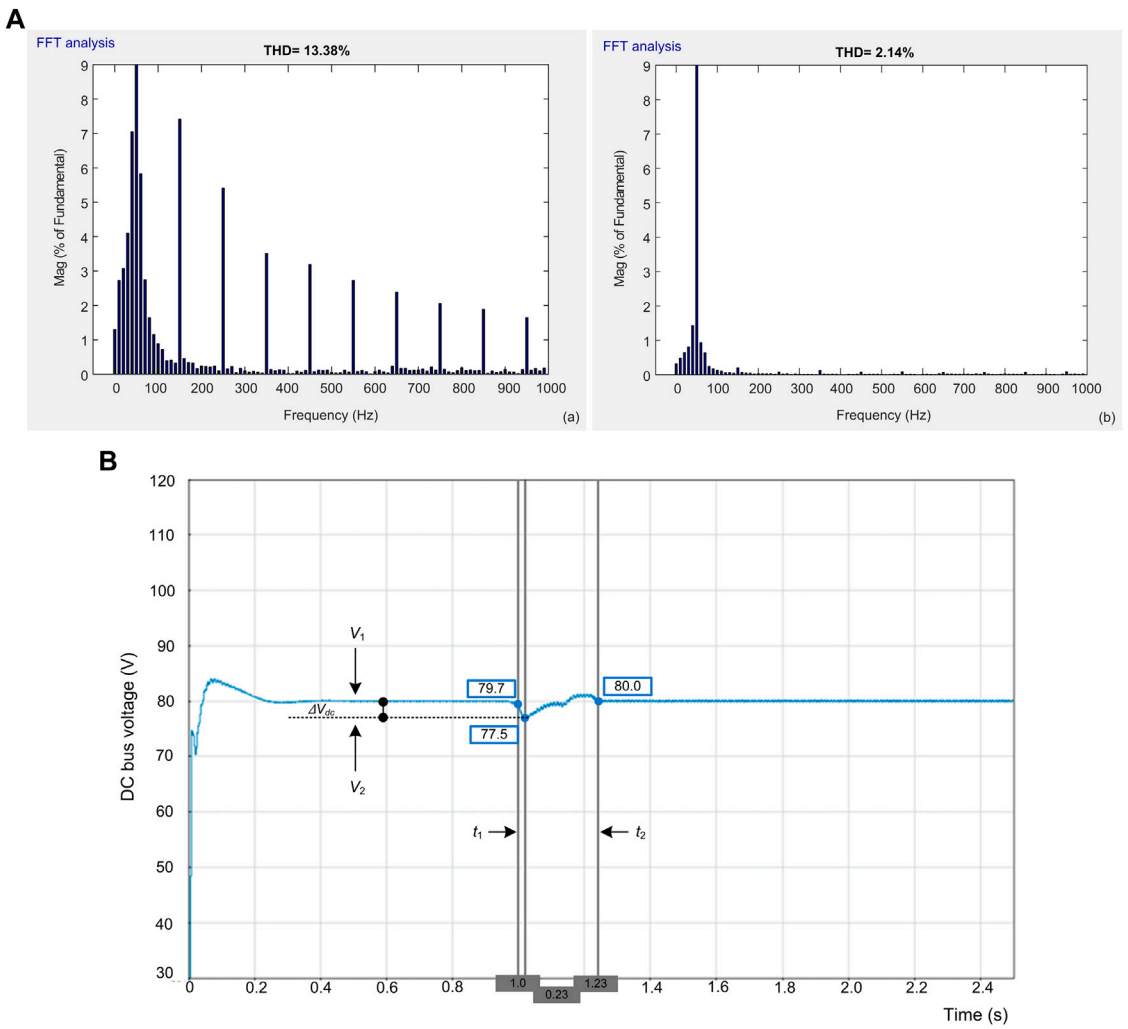

FIGURE 20
(A) THD analysis: (a) load current and (b) grid current. **(B)** M_p and T_r performance of DC bus voltage.

linear component of an AC load. In addition to compensating current harmonics and reactive power, the VSC delivers and absorbs real power to and from the utility grid in Figure 19Fb. Therefore, i_g in Figure 19Fc remains constant and the voltage and current of the AC grid are in phase. As a result, grid voltage and current are maintained with UPF. Figure 20A presents the harmonic spectra of i_L and i_g. A total harmonic distortion (THD) of 13.38% is measured on the current drawn by the non-linear load, while the current drawn by the grid is sinusoidal with a THD of 2.14% within the tolerances set by the IEEE-519 standard.

As illustrated at time t_1 in Figure 19Ba, the results are used to analyse the voltage overshoot and the settling time that occurs with a step change in load demand. The voltage overshoot equation is as follows:

$$M_P = \frac{\Delta V_{dc}}{V_{dc}} \times 100 \tag{25}$$

Figure 20B shows the change in voltage measured between V_1 and V_2 and the recovery time of voltage is measured between t_1 and t_2. The performance of the proposed system with the existing methods is presented in Table 5. Table 5 includes the peak overshoot (M_p), recovery time (T_r) of voltage, and grid THD compared to existing methods. Based on Table 5, the voltage overshoot is less and the DC link voltage requires less time to stabilise compared to the methods proposed in (Sathishkumar et al., 2012), (Manandhar et al., 2019), and (Tummuru et al., 2015b) techniques. Therefore, the proposed EMS provides less time to compute and has lower THD than existing methods.

6 Conclusion

An energy management strategy using ramp-rate control is proposed for a renewable grid-connected MG system with battery and supercapacitor as HESS. The effectiveness of the proposed strategy is demonstrated through the development and testing of a HIL setup. The main highlights are achieved using the proposed system mentioned below.

- Improved system reliability can be achieved by using ramp-rate control to smooth out fluctuations in PV power output.
- Since the amount of power generated from the battery depends on the ramp-rate control output, the charge/discharge rate of the battery to the controller is reduced and the power consumption of the battery is also reduced.
- Compared to existing methods, it achieves fast DC voltage regulation with a settling time of 230 ms.
- A grid-connected single-stage VSC can provide both current and voltage compensation.
- The SoC of ESSs ensures that all these characteristics are implemented within safe operating limits.
- HESS is used to assist both continuous and transient power applications. The purpose of SC device is also to minimize the current stress of BS and grid system.
- Also, the dynamic voltage compensation of the system is improved by SC, which also leads to an increase in system efficiency.

Therefore, the HIL experimental testbed results confirm that the proposed system can enhance local bus power quality under various conditions of PV, HESS, grid and loads. The controller enables efficient implementation of the EMS. There are numerous scenarios and control algorithms that can be tested using this test bench for research in the field of hybrid renewable energy MGs.

Due to their high costs and limited lifetime, future PV systems will rely heavily on ESS, which has a significant impact on the energy/economic balance of the PV system and plays a crucial role in the feasibility of PV systems in the future. Because of this, it is essential to carefully consider the ESS's energy capacity, losses, and cyclical deterioration. It is clear that if both the amount of energy stored in an ESS and the number of times it is charged and discharged are reduced, the cost of installing and maintaining an ESS will be reduced. Therefore, choosing a control approach to minimize fluctuations will be a significant decision. The transition between modes must be considered when designing effective management strategies for reliable and continuous system operation. Future work involves incorporating control approaches and algorithms to improve power quality in grid-integrated MG systems using HESS. PV power can be smoothed using advanced smoothing control techniques. Large-scale power applications can use smoothing control to sustain stable power and improve system power quality. Advanced HESS control approaches can help RES producers and system operators in numerous ways.

Data availability statement

The original contributions presented in the study are included in the article/supplementary material, further inquiries can be directed to the corresponding author.

Author contributions

Conceptualization, methodology, investigation, resources, data curation, writing—original draft preparation, GK; project administration, visualization, supervision, review, and editing, KP. Both authors have read and agreed to the published version of the manuscript.

Funding

This work was supported by the Department of Science and Technology (DST), Government of India (GOI) with the project grant SR/FST/ETI-420/2016(C) under FIST scheme.

Conflict of interest

The authors declare that the research was conducted in the absence of any commercial or financial relationships that could be construed as a potential conflict of interest.

Publisher's note

References

Alramlawi, M., and Li, P. (2020). Design optimization of a residential PV-battery microgrid with a detailed battery lifetime estimation model. *IEEE Trans. Ind. Appl.* 56 (2), 2020–2030. doi:10.1109/TIA.2020.2965894

Anilkumar, G., Chakradhar, A., Brahmendra Kumar, G. V., and Palanisamy, K. (2020). "Resource assessment and energy yield estimation for 160 MW solar-wind hybrid project using system advisory model," in IOP Conf. Ser, Mater. Sci. Eng, Vellore, India, 9 July 2020, 937, 012020. doi:10.1088/1757-899x/937/1/012020

Brahmendra Kumar, G. V., Kumar, G. A., Eswararao, S., and Gehlot, D. (2018). "Modelling and control of BESS for solar integration for PV ramp rate control," in Proceedings of the International Conference on Computation of Power, Energy, Information and Communication (ICCPEIC), Chennai, India, 28-29 March 2018 (IEEE), 368–374. doi:10.1109/ICCPEIC.2018.8525173

Brahmendra Kumar, G. V., and Palanisamy, K. (2019). "A review on microgrids with distributed energy resources," in *Innovations in power and advanced computing technologies (i-PACT)* (IEEE), 2019, 1–6. doi:10.1109/i-PACT44901.2019.8960189

Fu, Z., Li, B., and Wang, H. (2022). Real-time optimal scheduling of multi-microgrids considering renewable energy intermittency. *Front. Energy Res.* 10, 888156–888212. doi:10.3389/fenrg.2022.88815610.3389/fenrg.2022.888156

Gundumalla, V. B. K., and Eswararao, S. (2018). "Ramp rate control strategy for an islanded DC microgrid with hybrid energy storage system," in Proceedings of the 2018 4th International Conference on Electrical Energy Systems (ICEES), Chennai, India, 07-09 February 2018 (IEEE), 82–87. doi:10.1109/ICEES.2018.8442363

Hosseini, S. M., Carli, R., and Dotoli, M. (2021). Robust optimal energy management of a residential microgrid under uncertainties on demand and renewable power generation. *IEEE Trans. Autom. Sci. Eng.* 18 (2), 618–637. doi:10.1109/TASE.2020.2986269

Jiang, H., Wei, M., Zhao, Y., and Han, J. (2021). Design of decentralized adaptive sliding mode controller for the islanded AC microgrid with ring topology. *Front. Energy Res.* 9, 732997–733013. doi:10.3389/fenrg.2021.73299710.3389/fenrg.2021.732997

Karimi, Y., Oraee, H., Golsorkhi, M. S., and Guerrero, J. M. (2017). Decentralized method for load sharing and power management in a PV/Battery hybrid source islanded microgrid. *IEEE Trans. Power Electron.* 32 (5), 3525–3535. doi:10.1109/TPEL.2016.2582837

Kollimalla, S. K., Mishra, M. K., and Narasamma, N. L. (2014). Design and analysis of novel control strategy for battery and supercapacitor storage system. *IEEE Trans. Sustain. Energy* 5, 1137–1144. doi:10.1109/TSTE.2014.2336896

Kumar, G. V. B., Kaliannan, P., Padmanaban, S., Holm-Nielsen, J., and Blaabjerg, F. (2020). Effective management system for solar PV using real-time data with hybrid energy storage system. *Appl. Sci.* 10 (3), 1108–1115. doi:10.3390/app10031108

Kumar, G. V. B., and Palanisamy, K. (2020). A review of energy storage participation for ancillary services in a microgrid environment. *Inventions* 5 (4), 63–36. doi:10.3390/inventions5040063

Li, H., Fu, L., Zhang, Y., and Xiong, Y. (2022). A dynamic and cooperative control strategy for multi-hybrid energy storage system of DC microgrid based on SOC. *Front. Energy Res.* 9, 795513–795514. doi:10.3389/fenrg.2021.79551310.3389/fenrg.2021.795513

Li, Z., Chan, K. W., Hu, J., and Guerrero, J. M. (2021). Adaptive droop control using adaptive virtual impedance for microgrids with variable PV outputs and load demands. *IEEE Trans. Ind. Electron.* 68 (10), 9630–9640. doi:10.1109/TIE.2020.3022524

Mahmood, H., and Jiang, J. (2019). Decentralized power management of multiple PV, battery, and droop units in an Islanded microgrid. *IEEE Trans. Smart Grid* 10 (2), 1898–1906. doi:10.1109/TSG.2017.2781468

Manandhar, U., Ukil, A., Gooi, H. B., Tummuru, N. R., Kollimalla, S. K., Wang, B., et al. (2019). Energy management and control for grid connected hybrid energy storage system under different operating modes. *IEEE Trans. Smart Grid* 10 (2), 1626–1636. doi:10.1109/TSG.2017.2773643

Neto, P. B. L., Saavedra, O. R., and de Souza Ribeiro, L. A. (2018). A dual-battery storage bank configuration for isolated microgrids based on renewable sources. *IEEE Trans. Sustain. Energy* 9 (4), 1618–1626. doi:10.1109/TSTE.2018.2800689

Ouammi, A., Dagdougui, H., and Sacile, R. (2015). Optimal control of power flows and energy local storages in a network of microgrids modeled as a system of systems. *IEEE Trans. Control Syst. Technol.* 23 (1), 128–138. doi:10.1109/TCST.2014.2314474

Rahbar, K., Chai, C. C., and Zhang, R. (2018). Energy cooperation optimization in microgrids with renewable energy integration. *IEEE Trans. Smart Grid* 9 (2), 1482–1493. doi:10.1109/TSG.2016.2600863

Rosero, C. X., Velasco, M., Martí, P., Camacho, A., Miret, J., and Castilla, M. (2020). Active power sharing and frequency regulation in droop-free control for islanded microgrids under electrical and communication failures. *IEEE Trans. Ind. Electron.* 67 (8), 6461–6472. doi:10.1109/TIE.2019.293995910.1109/TIE.2019.2939959

Sahoo, S. K., Sinha, A. K., and Kishore, N. K. (2018). Control techniques in AC, dc, and hybrid AC-DC microgrid: A review. *IEEE J. Emerg. Sel. Top. Power Electron.* 6 (2), 738–759. doi:10.1109/JESTPE.2017.2786588

Sathishkumar, R., Kollimalla, S. K., and Mishra, M. K. (2012). "Dynamic energy management of micro grids using battery super capacitor combined storage," in Proceedings of the Annual IEEE India Conference (INDICON), Kochi, India, 07-09 December 2012, 1078–1083. doi:10.1109/INDCON.2012.6420777

Tummuru, N. R., Mishra, M. K., and Srinivas, S. (2015). Dynamic energy management of hybrid energy storage system with high-gain PV converter. *IEEE Trans. Energy Convers.* 30 (1), 150–160. doi:10.1109/TEC.2014.2357076

Tummuru, N. R., Mishra, M. K., and Srinivas, S. (2015). Dynamic energy management of renewable grid integrated hybrid energy storage system. *IEEE Trans. Ind. Electron.* 62 (12), 7728–7737. doi:10.1109/TIE.2015.2455063

Wang, D., Guan, X., Wu, J., Li, P., Zan, P., and Xu, H. (2016). Integrated energy exchange scheduling for multimicrogrid system with electric vehicles. *IEEE Trans. Smart Grid* 7 (4), 1762–1774. doi:10.1109/TSG.2015.2438852

Wang, G., Ciobotaru, M., and Agelidis, V. (2014). Power smoothing of large solar pv plant using hybrid energy storage. *IEEE Trans. Sustain. Energy* 5 (3), 834–842. doi:10.1109/TSTE.2014.2305433

Wang, Z., Chen, B., Wang, J., Begovic, M. M., and Chen, C. (2015). Coordinated energy management of networked microgrids in distribution systems. *IEEE Trans. Smart Grid* 6 (1), 45–53. doi:10.1109/tsg.2014.2329846

Wang, Z., Chen, B., Wang, J., and Kim, J. (2016). Decentralized energy management system for networked microgrids in grid-connected and islanded modes. *IEEE Trans. Smart Grid* 7 (2), 1097–1105. doi:10.1109/TSG.2015.2427371

Wu, D., Tang, F., Dragicevic, T., Vasquez, J. C., and Guerrero, J. M. (2015). A control architecture to coordinate renewable energy sources and energy storage systems in islanded microgrids. *IEEE Trans. Smart Grid* 6 (3), 1156–1166. doi:10.1109/TSG.2014.2377018

Xu, Q., Zhao, T., Xu, Y., Xu, Z., Wang, P., and Blaabjerg, F. (2020). A distributed and robust energy management system for networked hybrid AC/DC microgrids. *IEEE Trans. Smart Grid* 11 (4), 3496–3508. doi:10.1109/TSG.2019.2961737

Yi, Z., Dong, W., and Etemadi, A. H. (2017). A unified control and power management scheme for pv-battery-based hybrid microgrids for both grid-connected and islanded modes. *IEEE Trans. Smart Grid* 9 (6), 5975–5985. doi:10.1109/TSG.2017.2700332

Zia, M. F., Elbouchikhi, E., and Benbouzid, M. (2018). Microgrids energy management systems: A critical review on methods, solutions, and prospects. *Appl. Energy* 222, 1033–1055. doi:10.1016/j.apenergy.2018.04.103